Title

Measurement and modeling of ErAs:In0.53Ga0.47As nanocomposite photoconductivity for THz generation at 1.55 μm pump wavelength

Journal

Journal of Applied Physics, 116(1)

ISSN

0021-8979

Authors

Suen, JY
Krogen, PR
Preu, S
et al.

Publication Date

2014-07-07

DOI

10.1063/1.4886180

Peer reviewed

Measurement and modeling of ErAs:$In_{0.53}Ga_{0.47}As$ nanocomposite photoconductivity for THz generation at 1.55 μm pump wavelength

J. Y. Suen,[1,a)] P. R. Krogen,[2,b)] S. Preu,[3] H. Lu,[4] A. C. Gossard,[4] D. C. Driscoll,[4] and P. M. Lubin[5]

[1]*Department of Electrical and Computer Engineering, University of California, Santa Barbara, California 93106, USA*
[2]*Research Laboratory of Electronics, Massachusetts Institute of Technology, Cambridge, Massachusetts 02139, USA*
[3]*Department of Electrical Engineering and Information Technology, Technische Universität Darmstadt, Darmstadt 64283, Germany*
[4]*Materials Department, University of California, Santa Barbara, California 93106, USA*
[5]*Department of Physics, University of California, Santa Barbara, California 93106, USA*

(Received 22 April 2014; accepted 19 June 2014; published online 1 July 2014)

We present new high-resolution measurements of transient time-domain photoconductivity in ErAs:InGaAs superlattice nanocomposites intended for THz photoconductive switches and photomixers using a pure optical pump-probe method. We developed a model, using separate photocarrier trapping, recombination, and thermal reactivation processes, which very accurately fits the measurements. The measured material structures all exhibit a slow secondary decay process, which is attributed to thermal reactivation of the trapped carriers, either into the conduction band, or into high-energy defect states. We examined the influence of superlattice structure, dopants, DC bias, and temperature. Analysis shows that all of the THz energy produced by the photocarrier trapping and decay processes are at frequencies less than 1 THz, while the reactivation process only serves to create a large portion of the bias power dissipated. Energy higher than 1 THz must be created by a fast generation process or band-filling saturation. This allows pulsed THz generation even from a long-lifetime material. Pure optical pump-probe measurements are necessary to expose slow material processes, and eliminate the influence of electrical terminals and THz antennas. These measurements and modeling of THz photoconductive devices are necessary in order to optimize the output spectrum and power. [http://dx.doi.org/10.1063/1.4886180]

I. INTRODUCTION

Photoconductive switches (PC or Auston switches) and photomixers are efficient, compact, and solid-state methods for generating THz radiation. Typically, these devices are constructed with low-temperature grown GaAs (LT-GaAs), which has a bandgap of ~1.4 eV, corresponding to a wavelength of 870 nm. This necessitates the use of a costly 800 nm pump laser. However, development of epitaxially grown InGaAs with embedded ErAs nanoparticles has made it possible to develop these ultrafast photoconductive devices with narrow bandgap materials that can be excited with 1.55 μm radiation, thus making it possible to exploit lasers and fiber optics designed for optical communications. The availability of high-power fiber lasers and Er-doped fiber amplifiers (EDFAs) allows systems working at this wavelength to be lower in cost, more compact, and more efficient than comparable LT-GaAs based systems.

The materials studied are based on $In_{0.53}Ga_{0.47}As$ with embedded semimetallic ErAs nanoparticles. (One is designed as a superlattice structure with alternating $In_{0.53}Ga_{0.47}As$ and ErAs:$In_{0.52}Al_{0.48}As$ layers.) The ErAs deposition is designed not to form a complete surface coverage. ErAs instead nucleates into nanoparticles on the $In_{0.53}Ga_{0.47}As$ or $In_{0.52}Al_{0.48}As$ surface. The nanoparticles act as fast photocarrier traps, serving the same purpose as point defects in low-temperature grown materials. The ErAs contributes to a *n*-type background doping. In order to achieve high resistivity, the material needs to be compensated with a *p*-dopant, typically Be. All the sample structures were grown lattice-matched to InP:Fe substrates. Parameters, such as the doping and superlattice structure can be engineered in the growth processes to create a material with high electron mobility, dark resistivity, and short lifetime.[1] The material can be grown under typical molecular beam epitaxy (MBE) growth conditions and is very stable at high temperatures and thus can sustain annealing. These properties are necessary not only for THz photomixers and switches but are also important in high-speed PIN photodetectors, microwave detector diodes,[2,3] n-i-pn-i-p THz devices,[4] and cascaded multijunction solar cells.[5] For these applications, high-conductivity tunnel junction device contacts can be created by rare-earth nanoparticle composites.[6,7]

There has been previous work in the characterization of these materials and structures, including measurement of photocarrier lifetime[8–10] as well as the fabrication and characterization of photoconductive switches.[11–14] Most of the performance aspects of the previous work have been concerned with photocarrier lifetime as a function of a single

a)Author to whom correspondence should be addressed. Electronic mail: jsuen@ece.ucsb.edu
b)This research was performed while P. R. Krogen was at the Department of Electrical and Computer Engineering, University of California, Santa Barbara, California 93106, USA

structural variable, namely, doping concentration or superlattice period.

When modeling photoconductive THz generation, a single exponential decay process has been previously used to describe the carrier dynamics and lifetime in both LT-GaAs and ErAs:GaAs devices. A simple RC model of the antenna (R) and gap capacitance (C) is then used to predict device THz output.[15] Other models assume the time-domain laser pulse shape, either a Sech^2 or Gaussian, dominates.[16] More complex models use a combination of an exponential photocarrier recombination and Gaussian pulse[17] or create a complex time- and space-dependent differential equation formulation of the fields in the gap, which lacks an intuitive closed-form solution that can be easily fit to measured data.[18]

In previous models, the photocarrier decay has been modeled to be dependent solely on superlattice period. Specifically, if the process is diffusion limited, being governed by the transport of photocarriers from the InGaAs active layers into the ErAs recombination centers, then the photocarrier lifetime $\tau \propto \left(\frac{L}{2}\right)^2 D$, for superlattice period L and a diffusion rate D.[10] Another model is to treat the recombination process as being limited by available ErAs trap states, resulting in $\tau \propto L$, assuming ErAs deposition is constant. We found that these simple exponential decay models omit critical photocarrier dynamics, which affect both THz power generation and the thermal dissipation of the device. Measurements in this work have shown that photocarriers appear to recombine at a fast initial rate (~1–2 ps in a typical sample structure) before transitioning into a slow rate, on the order of tens of ps. Similar effects have been seen in ErSb:GaSb[19] and LT-GaAs materials.[20] A model in which photocarriers trap quickly and recombine slowly in LT-GaAs has been put forth based on time-domain THz measurements.[21] The presence of these carriers is believed to cause space-charge screening, shaping the THz pulse. Our measurement technique showed the presence of these trapped carriers in our samples without a bias field or THz antenna.

II. METHODOLOGY AND MODEL

In order to measure photocarrier lifetime, we utilized the optical pump-probe methodology described in Ref. 22. In our system, the optical power was generated by a 1550 nm ultrafast fiber laser (pulse full-width half-maximum FWHM = 210 fs, 25 MHz pulse repetition frequency, 15 mW average power, all measured at the fiber-to-freespace couplers). The pump pulse was 99% of this energy and the remaining 1% formed the probe pulse. The excitation conditions are comparable with those used in photomixing experiments for devices with a cross-sectional area in the range of 100 μm^2. This area is comparable with the laser spot size used in this work, which had a 10 μm diameter at the focus on the sample. The high power pump beam was chopped by a mechanical chopper wheel, and illuminated the sample at a 45° angle through a focusing fiber-to-freespace coupler. The low power probe beam was delayed with a stepper motor-controlled freespace delay line and then illuminated the sample perpendicular to the pump beam. A photodiode detected the transmitted probe energy and the signal was then amplified and demodulated with a lock-in amplifier. In order to block scattered pump light, a 50 μm pinhole was added in front of the photodiode, which greatly improved the signal-to-noise ratio. Because the optical pump-probe technique does not rely on an external field, the sample was tested bare. This eliminated the possibility of charge trapping or plasmon effects due to the gold contacts. The only exception was the one structure where a DC bias was applied in order to study non-diffusion limited transport. For these measurements, evaporated gold contacts, consisting of two trapezoids, which tapered to form two sides of a 25 μm square gap, were deposited. This measurement setup allowed high-resolution, long integration time measurements.

In optical pump-probe measurements, the material absorption coefficient is proportional to a large constant term plus a term proportional to the density of photoexcitable carriers. We consider this density equal to the sum of the carriers in the valence band. Since the total carrier density equals the sum of the valence band, conduction band, and trap state carrier density, and transmission and absorption sum to one, we can treat the differential optical transmission as being proportional to the sum of the conduction band and trap carrier density. In combination with our model, we can then determine the photocarrier trapping, recombination, and reactivation rates from the time-domain evolution of differential optical transmission.

Our model treats the photocarrier generation rate as having the same functional form as the ultrafast laser pulse, a Gaussian, with FWHM duration τ. These photocarriers are directly generated into conduction band states, which have photocarrier concentration n_c. The photocarriers then decay to the ErAs particle trap states with exponential rate λ_t. The photocarrier density in the trap states is denoted by n_t. While carriers are in the trap states, they either recombine to the valence band with rate λ_r or they are thermally activated back into the conduction band with rate λ_a. We expected the recombination and reactivation rates, λ_r and λ_a, to be slower than the trap rate λ_t. This can be expressed in the differential equations

$$\frac{dn_c}{dt} = -\lambda_t n_c + \lambda_a n_t + \exp\left((-4\ln 2)\frac{t^2}{\tau^2}\right), \qquad \frac{dn_t}{dt} = \lambda_t n_c - \lambda_a n_t - \lambda_r n_t. \tag{1}$$

There is no simple closed-form solution to this system, but in the case where λ_a is small relative to the other rates, the relation

$$n_c(t) \approx \frac{e^{-t(\lambda_t+\lambda_r)}\tau}{4(\lambda_t-\lambda_r)}\sqrt{\frac{\pi}{\ln 2}}\left(e^{t\lambda_r+\frac{\lambda_t^2}{4^2\ln 2}}(\lambda_a-\lambda_t+\lambda_r)\left(\mathrm{erf}\left(\frac{\lambda_t\tau^2-8t\ln 2}{4\tau\sqrt{\ln 2}}\right)-1\right)+\lambda_a e^{t\lambda_t+\frac{\lambda_t^2\tau^2}{4^2\ln 2}}\mathrm{erfc}\left(\frac{\lambda_r\tau^2-8t\ln 2}{4\tau\sqrt{\ln 2}}\right)\right) \tag{2}$$

was derived from Eq. (1) and very closely approximates the numerical solution.

To account for band-filling saturation, observed in nearly all of the samples as a flat top at the transmission peak, the function

$$R(t) = \min\{a\, n_c(t - t_0) + c\} \tag{3}$$

was fitted to the measured time-domain transmission data, where a, c, and t_0 are fitting constants. The fit parameters were then used with a numeric solution to Eq. (1) to compare with observed data. We can further account for the effects of the finite length of the probe pulse. If we assume the probe pulse is also a Gaussian function, it can be shown that the result of convolving the solution to Eq. (1) with the probe pulse is simply that the pulse FWHM parameter τ becomes the quadrature sum of the two Gaussian pulse lengths, while remaining rates are unchanged. Even though the laser had a pulse FWHM of 210 fs, the observed data had a optical generation time constant τ was around 1 ps and nearly uniform across all structures. The impact of the finite laser pulse is approximately 3% on τ and therefore negligible.

III. RESULTS AND DISCUSSION

We characterized six sample structures, denoted structures A through E, with varying parameters (Table I). Equation (3) was fit to the amplitude-normalized phototransmission traces with an extremely good agreement in all cases. The rates are shown in Table II, and all structures have the goodness of fitting parameter $R^2 \geq 0.9998$. Representative traces are depicted in Figure 1. The initial fast decay from the peak is approximately exponential at the trapping rate, while the longer tail is at the recombination rate. The transition region is related to the activation rate, so, as expected, $\lambda_t > \lambda_r > \lambda_a$. Structures A, C, and E are the baseline superlattice structures with Be compensation doping, varying in period from 20 nm to 5 nm. Structure B (Fig. 1(a)) was used in to fabricate THz switches in Ref. 13. In this structure, the ErAs recombination centers are deposited within an InAlAs layer, where ErAs forms deep traps. Optical absorption takes place in the adjacent InGaAs layers. Carriers must diffuse and tunnel into the ErAs nanoparticles through the 2.5 nm thick InAlAs barrier. This increases material resistivity at the expense of a slower recombination rate. Structure C was similarly used to create photoconductive switches in Ref. 12. Structure D (Fig. 1(b)) uses carbon as a dopant instead of Be. Carbon provides a more uniform doping in InGaAs over Be, which tends to diffuse through the material to surfaces and interfaces, but it is a shallower acceptor than Be. Finally, structure F (Fig. 1(c)) is a codeposited material where the ErAs nanoparticles are distributed throughout a single InGaAs active layer randomly. This sample was previously used in Ref. 11.

A. Photocarrier rates and model interpretation

The model closely fits the experimental data for all of the tested structures. Several significant trends that support the model, and the interpretation of the parameters can be identified. First, the percentage of all generated photocarriers that are observed to participate in the slow reactivation process varies between 1.9% and 185%, with all but the slow structures E and F remaining under unity (the highest of samples A–D was 61%). If the slow process represented trapping of carriers, then 100% of carriers generated should participate, and $\lambda_t = \lambda_a$, whereas our fitting shows $\lambda_t \gg \lambda_a$, discounting this possibility. A carrier participation rate of greater than 100% indicates that photocarriers cycle multiple times through the slow process. This is evidence against the hypothesis that the slow decay component observed is due to fast trapping sites filling up because it indicates carriers are continually being reactivated into the valence band.

In terms of the rates, the trapping rate λ_t is observed to be closely related to the ratio of ErAs to InGaAs. If we examine the ratio of ErAs deposition in monolayers (MLs) per nm InGaAs, structures B, A, and E have decreasing ratios of 0.046, 0.04, and 0.036, respectively, and increasing trapping time

TABLE I. Structure characteristics.

Structure	Superlattice periods	Superlattice unit	Compensation dopant (A-E δ doped)	Material structure
A	100	20 nm $In_{0.53}Ga_{0.47}As$ 0.8 Monolayer ErAs	Be (2×10^{13} cm^{-2})	
B	70	15 nm $In_{0.53}Ga_{0.47}As$ 2.5 nm $In_{0.52}Al_{0.48}As$ 0.8 Monolayer ErAs	Be (2×10^{13} cm^{-2})	
C	100	10 nm $In_{0.53}Ga_{0.47}As$ 0.8 Monolayer ErAs	Be (2×10^{13} cm^{-2})	
D	100	10 nm $In_{0.53}Ga_{0.47}As$ 0.8 Monolayer ErAs	C (2×10^{13} cm^{-2})	
E	100	5 nm $In_{0.53}Ga_{0.47}As$ 0.18 Monolayer ErAs	Be (1×10^{13} cm^{-2})	
F	Codeposited	Single 2 μm Er doped $In_{0.53}Ga_{0.47}As$ layer 7×10^{17} ErAs traps/cm^3	Be (5×10^{18} cm^{-3})	
Common characteristics		Semi-insulating InP:Fe substrate, (001) orientation		

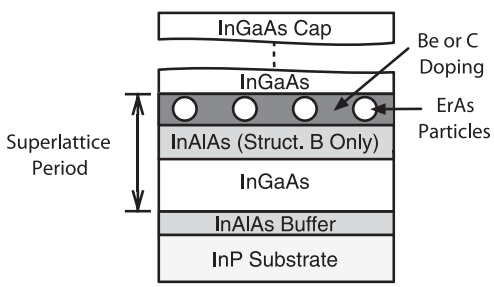

TABLE II. Fit parameters.

Structure	Trapping time constant λ_t^{-1} (ps)	Recombination time constant λ_r^{-1} (ps)	Reactivation time constant λ_a^{-1} (ps)	Gaussian FWHM τ (ps)	Percent energy in 2nd component
A	1.12	3.37	23.3	0.81	12.65
B	1.14	13.36	21.9	1.08	37.8
C	0.53	16.92	−34.8	1.13	32.7
D	0.52	0.85	43.5	1.04	1.9
E (biased from 0–5 kV/cm)	1.75	9.64	8.57	1.08	53.0
F cooled to					
77	3.31	24.97	17.1	1.31	59.3
160	2.05	9.92	8.38	1.92	54.2
170	2.03	8.74	7.91	1.76	52.5
180	1.69	7.18	5.51	1.88	56.6
200	2.75	13.03	11.8	1.33	52.3
300 K	2.49	15.01	8.12	1.39	64.9

constants of 1.14, 1.12, and 1.75 ps. Structures C and D have a high ratio of 0.08 monolayers per nm and have a correspondingly lower trapping time constant of about 0.52 ps. This is an indication that the initial photocarrier decay is indeed due to trapping by the ErAs nanoparticles, and the rate is determined by the availability of trap states. Carrier transport time is secondary to this effect as shown by the 5 nm-period structure E having a slower trap rate than the thicker structures C and D.

The thermal activation of trapped carriers occurs due to the shallow nature of the ErAs traps in InGaAs. The thermal activation rate, λ_a, was observed to be dependent on the depth of these traps. Without intentional doping, the 0.8 ML ErAs structures (all except Structure E) have a Fermi level that is only 15 meV below the conduction band edge, with a 70 meV activation energy. Structure E had a 0.18 ML ErAs deposition, corresponding to a state 20.2 meV above the conduction band edge and an 8 meV activation energy.[8] The compensation doping serves to lower the Fermi level, though the exact effects have only been measured for uniformly doped structures and not the delta-doping used in this study. Our results show that the 0.18 ML structure E has the highest λ_a, approximately three times greater than the 0.8 ML structures, even though it has a higher doping ratio (0.18 versus 0.08 Be atoms/Er atom). Thus, it appears that the increased availability of trapped carriers to thermally activate has a greater effect than the deeper trap level and activation energy.

Finally, all structures showed a photocarrier generation FWHM, τ, of about 1 ps. This is longer than that of the 220 fs laser pulse. We attribute the slower generation edge to the extremely high levels of photocarriers generated by the high laser flux, which has the potential to generate $\sim 10^{19}$ carriers/cm^3, approximately two orders of magnitude higher than the conduction band density of states of approximately 10^{17} cm^{-3} and one order greater than the valence band density of $\sim 10^{18}$ cm^{-3} in room temperature $In_{0.53}Ga_{0.47}As$. As carriers fill the conduction band, it is likely that the bandgap increases, lowering the optical cutoff wavelength. It is possible that this effect is reducing the bandwidth of the optical pulse, leading to time-domain broadening. We have also observed this effect with rise times of 1–2 ps measuring other material structures with a faster, higher power laser (80 fs FWHM, 35 kW peak).

B. Dopant-related effects

Dopant related effects are observed when comparing the Be-doped structure C with the carbon-doped structure D. The photocarrier trapping rates are identical, but when switching to carbon doping, the recombination rate is significantly increased, along with a reduction in thermal reactivation rate. The ability to localize the doping to the nanoparticles by carbon better compensates the *n*-type

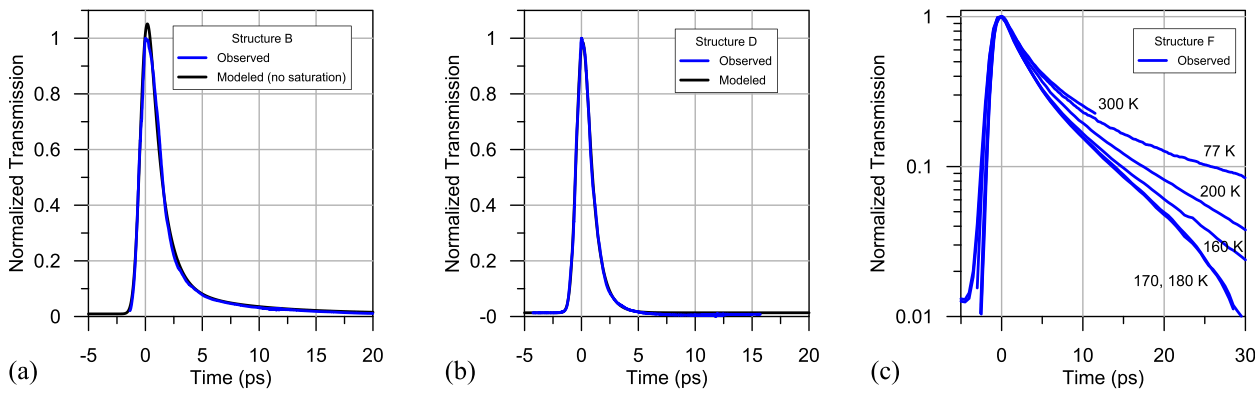

FIG. 1. Modeled and observed photoconductivity traces. (a) Structure B, a material similar to C but with an InAlAs barrier layer, (b) structure D a very fast carbon-doped structure, and (c) structure F cooled from room temperature to 77 K, showing the variance in secondary component lifetimes. The model for Structure B is shown without the max function in Eqn (3) to show the effects of band-filling saturation.

background of ErAs as well as prevents excess band-bending in the InGaAs which then results in generation of *p*-type carriers. The more favorable band structure accounts for the lower reactivation rate in the carbon-doped structure.

The codeposited structure F was previously used in Ref. 11 as a first-generation 1550 nm switch. Conversely, the doping in this material is non-localized and therefore the recombination and trapping rates are slow, and the reactivation rate high. ErAs particles tend to grow laterally with a 4 ML height in the superlattice structure. In the codeposited structure, they are more spherical with diameters varying from 2 to 30 nm. Because the Be doping is continuous throughout this codeposited structure, the regions between the nanoparticles become *p*-type, and band-bending can occur around the ErAs particles, leading to long material lifetimes, shallow trapping, and high dark currents.

C. Temperature and bias dependence

We explored behaviors as a function of temperature. Structure F was chosen due to its long lifetimes. Measurements were taken at 77 through 300 K (Fig. 1(c)). As the temperature increased, the secondary decay time decreased. From 77 K to 180 K, all of the material rates decreased. At 200 and 300 K, these rates increased from their minima. The behaviors of these rates are likely due to the combination of several opposing effects. It is known that material conductivity decreases continuously as the material is cooled to 77 K.[11] Hall effect measurements show that carrier mobility increases as temperature decreases from 300 K to beyond 18 K. I-V curves show an increasing resistivity down to at least 77 K, indicating that carrier concentration is decreasing at a higher rate than the increase in mobility.

A decrease in carrier concentration results in faster trapping and recombination rates by increasing the number of trap states available to each photocarrier. This is assisted by the higher carrier mobility, resulting in a shorter time for transport of carriers to the traps. Simultaneously, the lower temperature reduces thermal energy available, decreasing both electron and hole generation rates. In a classic Shockley-Read-Hall process, the lifetime increases as the material is cooled, proportionally to $T^{-\frac{3}{2}}$. Our data appear to suggest that the carrier concentration reduction and other lifetime shortening effects are dominant down to around 170 K. Below this temperature, the reduced thermal energy causes a rise in carrier lifetimes.

To further characterize the material, a DC bias field was applied to structure E, at field strengths from 500 to a maximum of 5000 V/cm, where material breakdown occurred. There was no detectable change in the photocarrier response (Table II). It was previously hypothesized that because the Be dopant is a shallow acceptor, it may emit electrons into the InGaAs by tunneling through the ErAs layer. Structure E is most susceptible to this effect due to its reliance on Be compensation to reduce the Fermi level below the conduction band edge. As there was no bias dependence, the data indicate that under both zero-bias and up to the breakdown voltage of these structures, the ionization energy of Be is sufficient to continue acting as an acceptor. One concern, however, is the ionization energy of carbon, which is about half of that of Be. The faster decay of the C-doped structure indicates that it performs well at zero-bias, but the performance under bias is unknown and warrants further study.

D. Photoinduced absorption transient

Of the materials tested, structure C was unique in that a negative differential transmission transient was observed. This property has previously been observed in ErAs:InGaAs,[9] LT-GaAs,[20] and LT-InP[23] structures. It has been attributed to carrier excitation from material defect states into states high into the conduction band.[23,24] Since the basis of the probe process is optical absorption by carriers, the negative transient indicates that either the concentration of carriers that may undergo an optically excited transition is above the equilibrium concentration or that the absorption cross-section for the carriers have increased. Our model shows that these absorptive carriers arise from a relatively slow process by a rate governed by trap state occupancy. One can hypothesize the source of these excess carriers to be dopant ionization or material defects. However, the effect is observed across three different material systems, though, it is only observed in a subset of our tested sample structures, specifically the structure with the fastest trapping rate but slowest recombination lifetime and thus highest trap occupancy time. We also note that this phenomenon has only been observed in optical measurements and we are unaware of observations of negative differential photoconductivity.

We believe that the photoinduced absorption phenomenon is due to second-photon excitation of the trapped carriers by the probe beam into higher-level states in the conduction band. This phenomenon requires high occupancy of trap states (Fig. 2). This is supported by measurements taken in Refs. 23 and 24, where optical wavelengths were varied. In Ref. 24, the LT-InGaAs structures exhibited increasing induced absorption as wavelength increased while optical power was held constant. Similar data from LT-InP in Ref. 23 showed

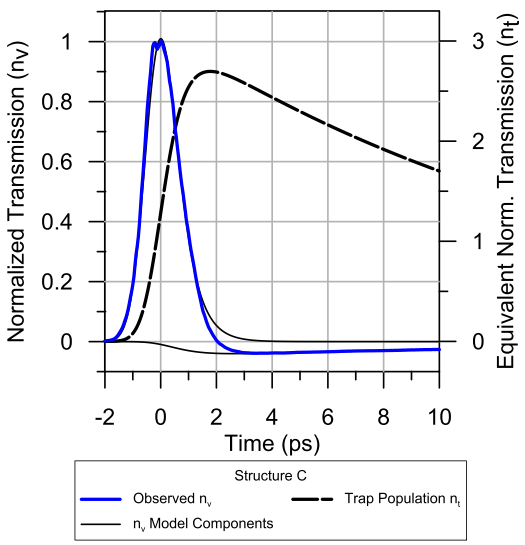

FIG. 2. Modeled photocarrier dynamics of structure C. The primary component of n_v, consisting of carrier generation and trapping, as well as the secondary component, caused by reactivation and second-photon absorption, is shown. The secondary component is dependent on trap population n_t, shown with the same relative units but scaled for display purposes.

that the absorption occurred only in a sample with faster trapping (grown at a lower temperature, suggesting higher trap densities). In that experiment, photoinduced absorption was observed at both long (860 nm) and short (570–650 nm) probe wavelengths, with a window of no absorption in between while the initial transient was unchanged. This trend indicates that second-photon excitation occurs not only where the photon energy is low, but with higher energy photons in order to reach even higher conduction band states. Second-photon excitation deep into the conduction band and saturation of the ErAs nanoparticles also give rise to the long decay at high power levels, as measured here, and as reported in Ref. 25. Carriers excited deep into the band slowly lose energy by releasing to the band edge before they can be effectively trapped. Furthermore, the absence of free states in the Er particles delays carrier trapping, resulting in long recombination lifetimes.

As an alternate hypothesis, it has been proposed that the negative differential is a result of two-photon excitation in the InP:Fe substrate. While this has been directly measured in Ref. 26, the transient observed here is much longer. Additionally, all of the structures were grown on identical substrates, and showed slow decay transients, but only one structure exhibited an absorptive transient. Therefore, two-photon absorption in the InP:Fe substrates cannot be the reason for the negative differential transmission observed in our study.

E. Summary

To summarize, our model correlates extremely well with all observed and expected behavior of 1550 nm wavelength-compatible ErAs:InGaAs photoconductors. Our high-resolution pure optical pump-probe measurements under zero bias eliminate effects, such as plasmon interaction with bias contacts and charge trapping. Unlike measurements of THz output, a pure optical measurement technique is able to easily measure slow transients, over tens of picoseconds, and does not rely on a model of a THz antenna. Dual exponential decay rates have been previously observed in a variety of LT-GaAs, LT-InP, and ErAs:InGaAs structures. The fast, initial decay has been attributed to the fast trapping of carriers, while the slow decay process has been identified as thermal reactivation process from trap states. The presence of this reactivation process is well supported based on the carrier population which undergoes slow decay, the coupling between the two processes and the close proximity of ErAs trap states to the conduction band edge which led to changes in rates as sample structure was varied.

IV. SYSTEMS ASPECTS: FREQUENCY OUTPUT AND POWER DISSIPATION

The most important characteristic of a photoconductive switch or photomixer in a system is the THz output spectrum. Of particular interest for these devices is the spectral roll-off at high frequencies, specifically the power emitted above 1 THz: frequencies that are difficult to reach with electronic devices. The effects of the carrier dynamics on output spectra are often modeled as a single pole.[15] Both the model and measured data presented here show roll-offs less than 20 dB/decade at low frequencies, and significantly higher roll-offs at higher frequencies, consistent with previous measurements.

If we assume an ideal antenna, the time derivative of the photoconductivity is proportional to the THz electric field emitted. (In the case of absorptive transients, the reactivated carriers still conduct but show excess absorption. To obtain an estimate of the photoconductivity, we simply take the absolute value of λ_a to ensure the transient is positive.) Figures 3(a) and 3(b) depict the derivative of the measured photocarrier concentration data and the model of structures B and C. Figures 3(c) and 3(d) show the same signals in the frequency domain, representing the THz output spectrum.

The first time-domain pulse in the E-field is generated by the laser-driven photocarrier generation process, whereas the second pulse is due to the trapping process. These processes generate THz power separately; it can be possible for a material with a slow trapping rate to generate power solely by a fast generation process. The much longer recombination lifetime does not directly affect THz generation since trapped carriers are at rest and do not generate current. Due to the $\sim$1 ps time constant of the trapping processes, the spectra that result from this effect roll off quickly, with very little power at frequencies above 1 THz. Rather, power generated at higher frequencies is caused by the fast photocarrier generation process and also assisted by the sharp cutoff in photocarrier generation due to bleaching saturation.

From the frequency spectra, we also examined the roll-off rate. Spot-frequency measurement and fitting of the roll-off have been used to derive device and material parameters.[11] Because the pulse shape is not strictly exponential, the components do not follow a single-pole 20 dB/decade decay. Structure B exhibited a -16.1 dB/decade from 192 to 500 GHz, whereas structure C decayed at -18.3 dB/decade from its peak at 200 GHz to 500 GHz. This is close to the -20 dB/decade over the same range derived from spot-frequency measurements in InGaAs material from Ref. 11 (which assumed a single-pole antenna rolloff). Looking over a wider bandwidth, structures B and C showed a -33.4 dB/decade and -32.9 dB/decade roll-off, respectively, from 200 to 1000 GHz. This was in better correspondence with the greater -25 dB/decade obtained via Fourier-Transform Infrared (FTIR) measurements on GaAs material from Ref. 16. We can conclude that the assumption of a single-pole material decay is inadequate.

Using our model, we can derive specific system design considerations necessary to maximize THz power and bandwidth. In most cases, thermal dissipation, rather than impact ionization, limits device output power. While the optical pulse repetition frequency will be limited by the relatively slow recombination rate, in practice thermal limits will be reached at far lower pulse rates. We can see that the conduction-band photocarriers generated by the slow trap reactivation process provide very little THz output power, yet lead to a potentially significant portion of the photocurrent and therefore device power dissipation. The proportion of the total time-integrated photoconductivity caused by the reactivated carriers is listed in Table II. The amounts range from 1 to 65% and are significant for almost all the

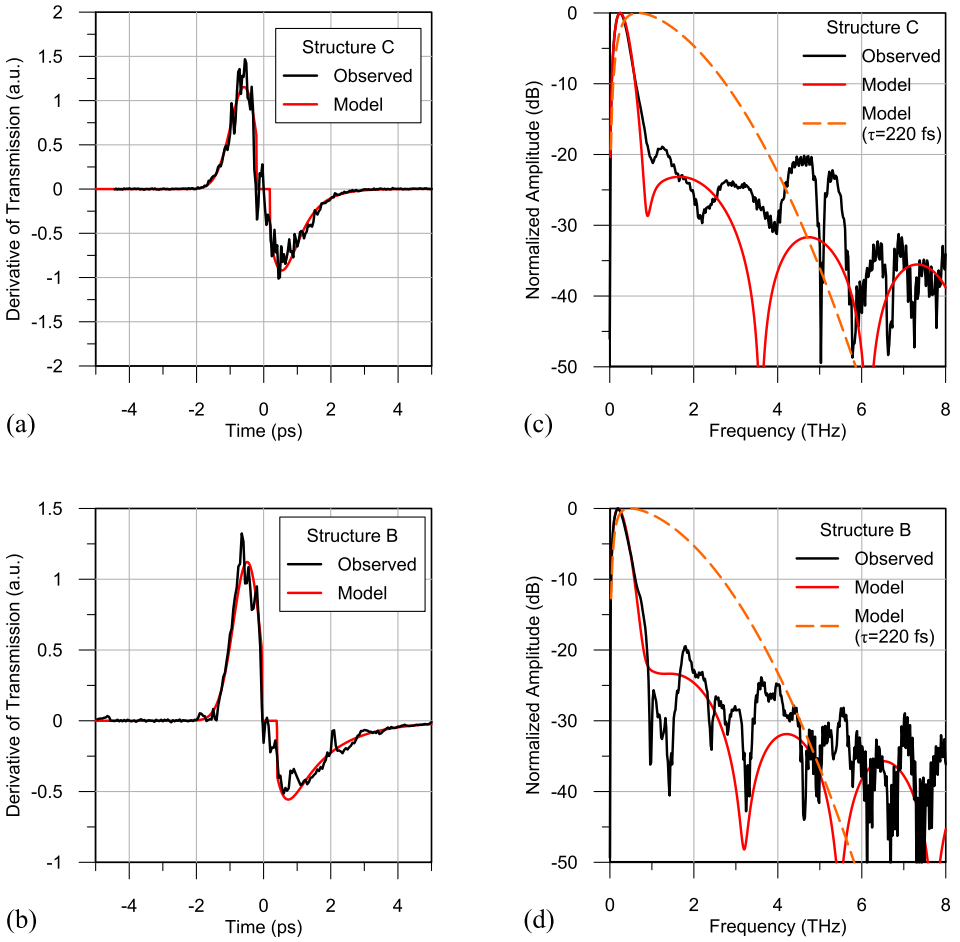

FIG. 3. (a) and (b) showing the time derivative of the observed and modeled photoconductivity for structures C (baseline) and B (InAlAs layer), respectively. This signal is proportional to the THz output power, assuming an ideal antenna. (c) and (d) shows the Fourier transform of (a) and (b). Without a fast risetime, THz output energy is fundamentally under 1 THz. Removing the optical pulse-slowing effects of high photocarrier densities, by assuming the generation duration, equal to the laser pulse duration, (dashed line) results in significant energy up to ~3 THz.

structures. The sample with the lowest reactivation component energy was structure D, which had very fast recombination and trapping rates, followed by structure A, which also benefitted from fast recombination times. The worst case was structure F at room temperature, which had a slow recombination rate combined with a slow trapping time. Cooling the sample resulted in relatively little variance in the percentage of reactivated photocarriers as the other material rates varied simultaneously. Other than the use of carbon doping, we did not identify a clear trend in the recombination rates based on material structure, carrier density and mobility measurements. This is an area for further study.

Also evident from the output spectra is the high roll-off of the model, with little power above 1 THz. For the tested structures, the band-filling saturation is responsible for the THz energy generation above this frequency, as shown by the sinc function nature of the model trace in Figures 3(c) and 3(d). Therefore, for photoconductive switches, excess laser power is detrimental in that it leads to long turn-on times and unnecessarily high level of photocurrent while the material is bleached for long periods of time.

If we set the photocarrier generation FWHM to match the laser ($\tau = 220$ fs), then THz output is extended to over 3 THz (Figures 3(c) and 3(d)). This is congruent with time-domain measurements of photoconductive switches made from structure B in Ref. 13. The fast, laser-driven photocarrier generation process combined with bleaching saturation explains why significant pulsed THz power can be generated by photoconductive switches in materials with lifetimes of many picoseconds, such as structure F in Ref. 11.

Most important for pulsed operation is a large dark resistance, in order to avoid thermal destruction due to the electrical power delivered. In contrast, continuous-wave (CW) photomixers must feature both high resistance and short lifetime materials and structures: saturation in these devices leads to harmonic generation, and unlike switches, the CW mode of operation does not allow for a material recovery time. In pulsed operation, the material can relax between two pulses (typically an interval of several microseconds). For CW operation, the carriers have to recombine within a fraction of the THz period, since the photoconductor is continuously excited.

V. CONCLUSIONS

We have measured and modeled the ultrafast photocarrier response based on coupled trapping, reactivation, and recombination processes in ErAs:InGaAs superlattice structures. Our model closely matches the observed pure optical pump-probe data. The features seen here have been widely observed in ErAs:InGaAs as well as LT-GaAs and LT-InP photoconductive devices. Fast photoconductivity decay is caused by carrier trapping, while recombination and thermal reactivation processes combine to form a slow secondary transient, which may be transmissive or absorptive, and is essentially impossible to observe by measuring THz energy.

This model was well supported by observations across a broad range of structural configurations as well as temperature and DC bias-dependent measurements. We found that all of the THz output power over 1 THz was fundamentally caused by the fast photocarrier generation process, assisted by the abrupt cutoff of bleaching saturation. A slow transient was caused by the thermal activation of the trapped carriers, lengthened by a long recombination lifetime. This reactivation created as much as 65% of the total thermal dissipation and is a limiting factor in increasing THz output power. It was observed that the photocarrier generation process was consistently lengthened to five times the optical pulse width. This appears to be due to the high optical flux causing filling of the conduction band, leading to cutoff of the long-wavelength components of the optical pulse, effectively broadening the pulse. The model and analysis present paths to further optimize material performance, potentially by increasing ErAs nanoparticle deposition and reducing superlattice period. This has the advantages of both increasing the trapping rate, by providing more ErAs trap states, and increasing the distance of trap states from the conduction band edge, thus decreasing carrier reactivation. Alternative compensation dopants, such as carbon are worthy of further study. Finally, the results of our study show that time-domain photoconductivity measurements, with representative laser flux, must be made in order to fully optimize power generation from THz photoconductive switches.

ACKNOWLEDGMENTS

The authors wish to acknowledge the bias-dependent effects that were proposed by E. R. Brown. This work was partially supported by the MRSEC Program of the National Science Foundation under Award No. DMR-0520415.

[1]D. C. Driscoll, M. P. Hanson, and A. C. Gossard, "Carrier compensation in semiconductors with buried metallic nanoparticles," J. Appl. Phys. **97**, 016102 (2004).
[2]A. C. Young, J. D. Zimmerman, E. R. Brown, and A. C. Gossard, "Semimetal-semiconductor rectifiers for sensitive room-temperature microwave detectors," Appl. Phys. Lett. **87**, 163506 (2005).
[3]E. R. Brown, A. C. Young, J. E. Bjarnason, J. D. Zimmerman, A. C. Gossard, and H. Kazemi, "Millimeter and sub-millimeter wave performance of an ErAs:InAlGaAs Schottky diode coupled to a single-turn square spiral," Int. J. High Speed Electron. Syst. **17**, 383 (2007).
[4]S. Preu, F. H. Renner, S. Malzer, G. H. Döhler, L. J. Wang, M. Hanson, A. C. Gossard, T. L. J. Wilkinson, and E. R. Brown, "Efficient terahertz emission from ballistic transport enhanced n-i-p-n-i-p superlattice photomixers," Appl. Phys. Lett. **90**, 212115 (2007).
[5]J. M. O. Zide, A. Kleiman-Schwarsctein, N. C. Strandwitz *et al.*, "Increased efficiency in multijunction solar cells through the incorporation of semimetallic ErAs nanoparticles into the tunnel junction," Appl. Phys. Lett. **88**, 162103 (2006).
[6]R. Salas *et al.*, "Compositional grading of InxGa1-xAs/GaAs tunnel junctions enhanced by ErAs nanoparticles," Proc. SPIE **8106**, 81060P (2011).
[7]S. Preu *et al.*, "Efficient III–V tunneling diodes with ErAs recombination centers," Semicond. Sci. Technol. **25**, 115004 (2010).
[8]D. C. Driscoll, M. Hanson, C. Kadow, and A. C. Gossard, "Electronic structure and conduction in a metal-semiconductor digital composite: ErAs:InGaAs," Appl. Phys. Lett. **78**(12), 1703 (2001).
[9]D. C. Driscoll, M. P. Hanson, A. C. Gossard, and E. R. Brown, "Ultrafast photoresponse at 1.55 um in InGaAs with embedded semimetallic ErAs nanoparticles," Appl. Phys. Lett. **86**, 051908 (2005).
[10]F. Ospald, D. Maryenko, K. von Klitzing *et al.*, "1.55 um ultrafast photoconductive switches based on ErAs:InGaAs," Appl. Phys. Lett. **92**, 131117 (2008).
[11]K. K. Williams, Z. D. Taylor, J. Y. Suen *et al.*, "Toward a 1550 nm InGaAs photoconductive switch for terahertz generation," Opt. Lett. **34**(20), 3068 (2009).
[12]A. Schwagmann, Z.-Y. Zhao, and F. Ospald, "Terahertz emission characteristics of ErAs:InGaAs-based photoconductive antennas excited at 1.55 um," Appl. Phys. Lett. **96**, 141108 (2010).
[13]S. Preu, M. Mittendorff, H. Lu, H. B. Weber, S. Winnerl, and A. C. Gossard, "1550 nm ErAs:In(Al)GaAs large area photoconductive emitters," Appl. Phys. Lett. **101**, 101105 (2012).
[14]R. J. B. Dietz, M. Gerhard, D. Stanze, M. Koch, B. Sartorius, and M. Schell, "THz generation at 1.55 μm excitation: Six-fold increase in THz conversion efficiency by separated photoconductive and trapping regions," Opt. Express **19**(27), 25911 (2011).
[15]E. R. Brown, "THz generation by photomixing in ultrafast photoconductors," Int. J. High Speed Electron. Syst. **13**, 497 (2003).
[16]J. Y. Suen, W. Li, Z. D. Taylor, and E. R. Brown, "Characterization and modeling of a terahertz photoconductive switch," Appl. Phys. Lett. **96**, 141103 (2010).
[17]L. Deng, W.-Z. Lin, Z. R. Sun, and Z. G. Wang, "Response characteristic of femtosecond LT-GaAs photoconductive switches at different voltage biases," J. Phys. D: Appl. Phys. **42**, 245103 (2009).
[18]N. Khiabani, Y. Huang, Y.-C. Shen, and S. Boyles, "Theoretical modeling of a photoconductive antenna in a terahertz pulsed system," IEEE Trans. Antennas Propag. **61**(4), 1538 (2013).
[19]M. P. Hanson, D. C. Driscoll, J. D. Zimmerman, A. C. Gossard, and E. R. Brown, "Subpicosecond photocarrier lifetimes in GaSb/ErSb nanoparticles at 1.55 um," Appl. Phys. Lett. **85**, 3110 (2004).
[20]E. S. Harmon, M. R. Melloch, J. M. Woodall, D. D. Nolte, N. Otsuka, and C. L. Chang, "Carrier lifetime versus anneal in low temperature growth GaAs," Appl. Phys. Lett. **63**, 2248 (1993).
[21]G. Loata, M. D. Thomson, T. Löffler, and H. G. Roskos, "Radiation field screening in photoconductive antennae studied via pulsed terahertz emission spectroscopy," Appl. Phys. Lett. **91**, 232506 (2007).
[22]M. Sukhotin, E. R. Brown, and D. Driscoll, "Picosecond photocarrier-lifetime in ErAs:InGaAs at 1.55 um," Appl. Phys. Lett. **83**(19), 3921 (2003).
[23]Y. Kostoulas, L. J. Waxer, I. A. Walmsley *et al.*, "Femtosecond carrier dynamics in low-temperature-grown indium phosphide," Appl. Phys. Lett. **66**(14), 1821 (1995).
[24]P. W. Juodawlkis, D. T. McIntruss, and S. E. Ralph, "Ultrafast carrier dynamics and optical nonlinearities of low-temperature-grown InGaAs/InAlAs multiple quantum wells," Appl. Phys. Lett. **69**, 4062 (1996).
[25]G. Segschneider, F. Jacob, T. Löffler, and H. G. Roskos, "Free-carrier dynamics in low-temperature-grown GaAs at high excitation densities investigated by time-domain terahertz spectroscopy," Phys. Rev. B **65**(12), 125205 (2002).
[26]D. Vignaud, J. F. Lampin, and F. Mollot, "Two-photon absorption in InP substrates in the 1.55 μm range," Appl. Phys. Lett. **85**, 239 (2004).